Publication Year	2019
Acceptance in OA	2020-12-18T11:15:09Z
Title	Identification of strontium in the merger of two neutron stars
Authors	Watson, Darach, Hansen, Camilla J., Selsing, Jonatan, Koch, Andreas, Malesani, Daniele B., Andersen, Anja C., Fynbo, Johan P. U., Arcones, Almudena, Bauswein, Andreas, COVINO, Stefano, GRADO, ANIELLO, Heintz, Kasper E., HUNT, Leslie Kipp, Kouveliotou, Chryssa, Leloudas, Giorgos, Levan, Andrew J., Mazzali, Paolo, PIAN, Elena
Publisher's version (DOI)	10.1038/s41586-019-1676-3
Handle	http://hdl.handle.net/20.500.12386/28999
Journal	NATURE
Volume	574

Article

Identification of strontium in the merger of two neutron stars

https://doi.org/10.1038/s41586-019-1676-3

Received: 8 February 2018

Accepted: 14 August 2019

Darach Watson[1,2*], Camilla J. Hansen[1,3,20], Jonatan Selsing[1,2,20], Andreas Koch[4], Daniele B. Malesani[1,2,5], Anja C. Andersen[1], Johan P. U. Fynbo[1,2], Almudena Arcones[6,7], Andreas Bauswein[7,8], Stefano Covino[9], Aniello Grado[10], Kasper E. Heintz[1,2,11], Leslie Hunt[12], Chryssa Kouveliotou[13,14], Giorgos Leloudas[1,5], Andrew J. Levan[15,16], Paolo Mazzali[17,18] & Elena Pian[19]

Half of all of the elements in the Universe that are heavier than iron were created by rapid neutron capture. The theory underlying this astrophysical r-process was worked out six decades ago, and requires an enormous neutron flux to make the bulk of the elements[1]. Where this happens is still debated[2]. A key piece of evidence would be the discovery of freshly synthesized r-process elements in an astrophysical site. Existing models[3–5] and circumstantial evidence[6] point to neutron-star mergers as a probable r-process site; the optical/infrared transient known as a 'kilonova' that emerges in the days after a merger is a likely place to detect the spectral signatures of newly created neutron-capture elements[7–9]. The kilonova AT2017gfo—which was found following the discovery of the neutron-star merger GW170817 by gravitational-wave detectors[10]—was the first kilonova for which detailed spectra were recorded. When these spectra were first reported[11,12], it was argued that they were broadly consistent with an outflow of radioactive heavy elements; however, there was no robust identification of any one element. Here we report the identification of the neutron-capture element strontium in a reanalysis of these spectra. The detection of a neutron-capture element associated with the collision of two extreme-density stars establishes the origin of r-process elements in neutron-star mergers, and shows that neutron stars are made of neutron-rich matter[13].

The most detailed information yet available for a kilonova comes from a series of spectra of AT2017gfo taken over several weeks with the medium-resolution, ultraviolet (320 nm) to near-infrared (2,480 nm) spectrograph X-shooter, mounted at the Very Large Telescope at the European Southern Observatory. These spectra[11,12] allow us to track the evolution of the kilonova's primary electromagnetic output from 1.5 days until 10 days after the event. Detailed modelling of these spectra has yet to be done, owing to limited understanding of the phenomenon and the expectation that a very large number of moderate to weak lanthanide lines with unknown oscillator strengths would dominate the spectra[14,15]. Despite this expected complexity we sought to identify individual elements in the early spectra, because these spectra are well reproduced by relatively simple models[11].

The first-epoch spectrum can be reproduced over the entire observed spectral range by using a single-temperature blackbody with an observed temperature of approximately 4,800 K. The two major deviations short of 1 μm from a pure blackbody are due to two very broad absorption components (with widths of roughly 0.2c, where c is the speed of light). These components are centred at about 350 nm and 810 nm (Fig. 1). The shape of the ultraviolet absorption component is not well constrained because it lies close to the edge of our sensitivity limit and may simply be cut off below about 350 nm. The presence of the absorption feature at 810 nm in this epoch has been noted previously[11,12].

The fact that the spectrum is very well reproduced by a single-temperature blackbody in the first epoch suggests a population of states close to local thermal equilibrium (LTE). We therefore use three separate methods of increasing complexity first to determine, without too many assumptions, the most likely origin of the spectral features, and then to self-consistently model and test our conclusion. These three methods are: first, our own LTE spectral-synthesis code; second, the LTE line-analysis and spectrum-synthesis code MOOG[16]; and third, the moving-plasma radiative-transfer code TARDIS[17] (see Methods). We use a variety

---

[1]Niels Bohr Institute, University of Copenhagen, Copenhagen, Denmark. [2]Cosmic Dawn Center (DAWN), Copenhagen, Denmark. [3]Max-Planck-Institut für Astronomie, Heidelberg, Germany. [4]Zentrum für Astronomie der Universität Heidelberg, Astronomisches Rechen-Institut, Heidelberg, Germany. [5]DTU Space, National Space Institute, Technical University of Denmark, Kongens Lyngby, Denmark. [6]Institut für Kernphysik, Technische Universität Darmstadt, Darmstadt, Germany. [7]GSI Helmholtzzentrum für Schwerionenforschung GmbH, Darmstadt, Germany. [8]Heidelberger Institut für Theoretische Studien, Heidelberg, Germany. [9]Istituto Nazionale di Astrofisica (INAF)/Brera Astronomical Observatory, Merate, Lecco, Italy. [10]INAF/Osservatorio Astronomico di Capodimonte (OACN), Naples, Italy. [11]Centre for Astrophysics and Cosmology, Science Institute, University of Iceland, Reykjavík, Iceland. [12]INAF/Osservatorio Astrofisico di Arcetri, Firenze, Italy. [13]Department of Physics, The George Washington University, Washington, DC, USA. [14]Astronomy, Physics and Statistics Institute of Sciences (APSIS), Washington, DC, USA. [15]Department of Physics, University of Warwick, Coventry, UK. [16]Department of Astrophysics/IMAPP, Radboud University Nijmegen, Nijmegen, The Netherlands. [17]Astrophysics Research Institute, Liverpool John Moores University, Liverpool, UK. [18]Max-Planck Institute for Astrophysics, Garching, Germany. [19]INAF, Astrophysics and Space Science Observatory, Bologna, Italy. [20]These authors contributed equally: Camilla J. Hansen, Jonatan Selsing. *e-mail: darach@nbi.ku.dk

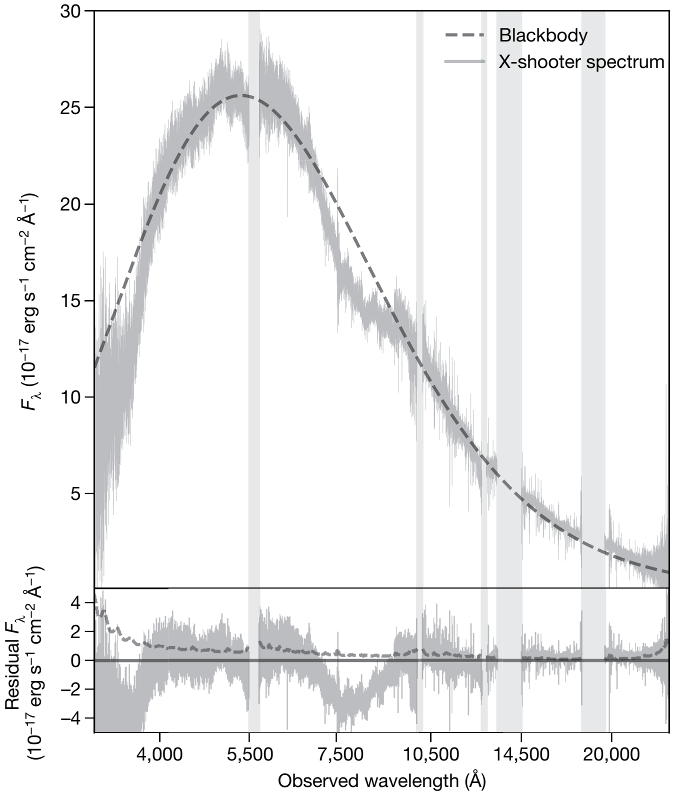

Fig. 1 | Spectrum of the kilonova AT2017gfo, showing broad absorption features. The spectrum shown was taken with the spectrograph X-shooter 1.5 days after the neutron-star merger GW170817. The dashed black line in the upper panel is the blackbody component of a blackbody model with broad absorption lines (see main text). The residuals of data minus blackbody are shown in the lower panel, with the dashed grey line indicating the 1σ uncertainty on each spectral bin. The data in the sections overplotted with grey bars are affected by telluric features or are poorly calibrated regions and are not included in the fit. F_λ is the flux per unit wavelength.

of spectral-line lists for these codes, all of which yield consistent results. For our own LTE code, we adopt a fiducial temperature of 3,700 K, which is our final model's best-fit temperature corrected by the Doppler factor (−0.23) of the absorption features that we determine below; changing the temperature of our LTE model in the range 3,700–5,100 K does not markedly affect our results.

To identify the absorption features, we seek lines with wavelengths blueshifted by 0.1–0.3*c*, corresponding approximately to 390–500 nm and 900–1,160 nm in the rest frame (see Methods). The lines will also be broadened with an observed width that depends on the velocity and geometry. For spherically expanding ejecta, the line broadening will be similar to the expansion velocity of the gas. We do not attempt a detailed geometric model here because it depends on assumptions about the geometry of the gas and the wavelength-dependent opacity, with substantial relativistic and time-delay corrections.

We adopt an initially agnostic view of the expected abundances. We use solar r-process abundance ratios (the total solar abundances of heavy elements[18] with s-process elements subtracted[19]), as well as abundances from two metal-poor stars that are old enough to be dominated by the r-process in their neutron-capture abundances[20,21]. These three sets span a wide range in their ratios of light-to-heavy r-process abundances (Fig. 2). We also produce absorption spectra for each element individually (Extended Data Figs. 1, 2).

Our LTE models using abundances from a solar-scaled r-process and metal-poor stars all show that Sr produces a strong feature centred at an observed wavelength of roughly 800 nm, as well as features at wavelengths shorter than around 400 nm, for our adopted blueshift (Fig. 3; see also Extended Data Fig. 3). The restframe wavelengths of the longer-wavelength features are 1,000–1,100 nm. It is worth noting that Sr is typically considered an s-process element because only about 30% of the cosmic (solar) abundance is produced by the r-process[18,19]. For this reason it has not always been considered in kilonova simulations. However, it is one of the more abundant r-process elements, accounting for at least a few per cent by mass of all such elements[19]. Of all of the r-process elements, Sr displays by far the strongest absorption features in this region of the spectrum (Extended Data Figs. 2, 3). Ba produces strong absorption, as do the lanthanide elements, but only in the optical region at wavelengths shorter than about 650 nm. The spectral features that we observe can therefore only be due to Sr, an element produced near the first r-process peak.

The 810-nm feature was previously proposed[12] to originate in absorption from Cs I and Te I. This identification can now be ruled out, because neither Cs I nor Te I produces strong lines in a plasma at this temperature (Extended Data Fig. 3). Much stronger lines would be expected from the ions of other elements that are co-produced with Cs (atomic number $Z = 55$) (for example, the lines from La II; see Methods).

The most abundant r-process elements are those in the first peak (Fig. 2)—elements with mass numbers (A) of around 80—and of these, it is Sr, Y ($Z = 39$) and Zr ($Z = 40$) that are easily detected in a low-density, roughly 4,000-K thermal plasma, because these elements have low excitation potentials for their singly charged ions. Seen in this context, the detection of Sr in AT2017gfo is not surprising, despite prior expectations that the spectra would be dominated by heavier elements[14,22]. Furthermore, the atomic levels in Sr that give the absorption lines observed at 810 nm are metastable. Photo-excitation can increase the population in these states, strengthening the 810-nm feature markedly[23] compared with the resonance blue/near-ultraviolet absorption lines. Ba and the lanthanide series contribute substantially to the total opacity of r-process material in the optical region of the spectrum (Fig. 2), yet we do not detect strong optical features. We cannot on this basis, however, easily exclude the presence of elements with mass numbers of more than 140 or so. Even if we could exclude the presence of heavier elements in the outer layers of the thermal, expanding cloud, there is no way from these early spectra of excluding the possibility that such elements could exist at lower depths or in an obscured component.

Given that a simple r-process abundance LTE model can account well for the first-epoch spectrum, we expand it to the subsequent three epochs, while the kilonova is still at least partially blackbody like. With a freely expanding explosion we expect to begin observing P Cygni lines once the outer absorbing 'atmosphere' begins to become more optically thin and attain a substantial physical radius with respect to the photospheric radius. We fit the first four epochs as a blackbody with P Cygni lines from Sr. We fit only the strongest lines in order to reduce our computational time to a manageable level, as these lines provide most of the opacity at these wavelengths. These fits are shown in Fig. 4 and offer a compelling reproduction of the spectra at all three epochs. The P Cygni model has free parameters for the velocities of the photosphere and atmosphere, which change the shape of the profile. The fit is remarkable given its simplicity and our lack of knowledge of the system geometry. We note that P Cygni emission components are always centred close to the rest wavelength of the spectral lines, so the observed wavelength of the emission line is not a free parameter. The most prominent emission component observed throughout the spectral series is centred close to 1,050 nm, and the weighted restframe centre of the near-infrared lines from Sr is also 1,050 nm. This adds to our confidence in the line identification based on the simple thermal r-process absorption model.

We further confirm our results using TARDIS ('temperature and radiative diffusion in supernovae'), extending this code's atomic database to include elements up to $_{92}$U by using the latest Kurucz line list[24] with its 2.31 million lines. Our TARDIS models produce results very similar to

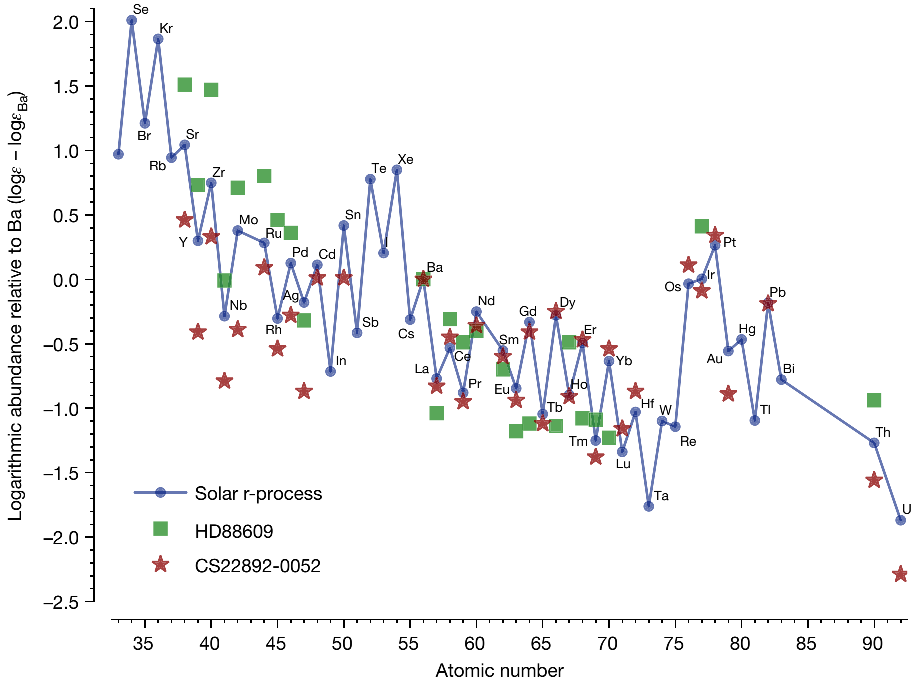

Fig. 2 | Abundances of elements produced by the r-process. Relative r-process abundances (ε) normalized to the Ba abundance are shown for the Sun and for two metal-poor stars—one, CS 22892–052, rich in heavy r-process elements[31,32], and the other, HD 88609, rich in light r-process elements[20]. These are the abundances of the elements used in the inset of Fig. 3.

our static-code models, reproducing the spectra well (Extended Data Fig. 6). In particular, the P Cygni emission/absorption structure is well reproduced as expected, confirming our LTE and MOOG modelling, and showing Sr dominating the features around 1 µm.

Given our detection of Sr, it is clearly important to consider lighter r-process elements in addition to the lanthanide elements in shaping the kilonova emission spectrum. Observations of abundances in stars in dwarf galaxies[6] suggest that large amounts of Sr are produced together

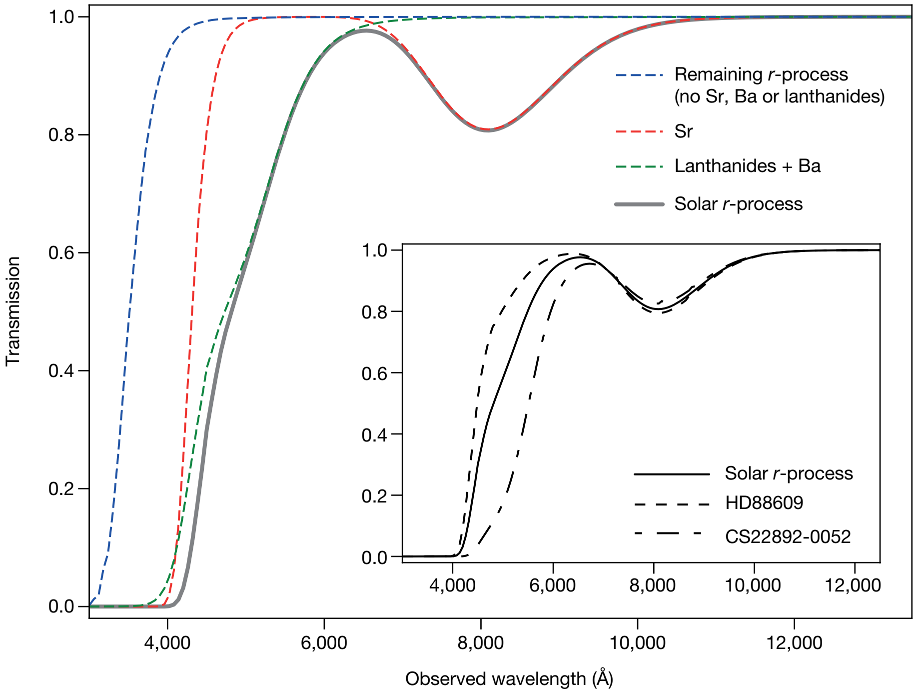

Fig. 3 | Thermal r-process-element transmission spectrum. These spectra are based on the lines formed in a gas in local thermal equilibrium with a temperature of 3,700 K and an electron density of 10^7 cm^{-3}, broadened by 0.2c and blueshifted by 0.23c. The spectrum produced by a solar r-process abundance ratio is plotted as a solid line. Contributions due to Sr (red dashed line), Ba and the lanthanides (green dashed line) and the remaining r-process elements (blue dashed line) are also shown. Inset, spectra resulting from a solar r-process abundance ratio (solid line), and from the abundance ratios of the metal-poor stars HD 88609 (dashed line)[20] and CS 22892–052 (dash-dotted line)[31,32].

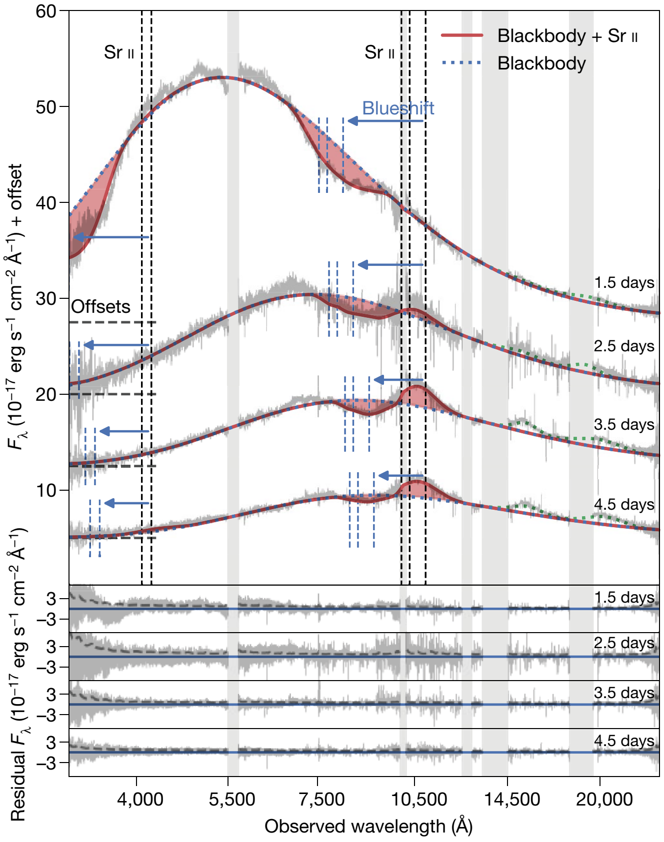

Fig. 4 | Spectral series of AT2017gfo 1.5–4.5 days after the merger. Data are shown in grey and have been smoothed slightly. Top panel, a model (solid red lines) consisting of a blackbody (blue dotted lines) with P Cygni profiles (red transparent fill) for the Sr lines. The rest (vertical black dashed lines) and observed (vertical blue dashed lines) positions of the model's Sr lines are shown, with the blueshift indicated by arrows. Green dotted lines show the Gaussian emission profiles added to ensure the overall continuum is not biased. A vertical offset has been applied to each spectrum for clarity, with zero flux indicated by the dashed horizontal line segments. Bottom panels show the residuals between model and data.

with Ba ($Z = 56$) in infrequent events, implying the existence of a site that produces both light and heavy r-process elements together in quantity, as found in some models[25,26]. This is consistent with our spectral analysis of AT2017gfo and analyses of its lightcurve[27,28]. Together with the differences observed in the relative abundances of r-process Ba and Sr in stellar spectra[29], this suggests that the relative efficiencies of light and heavy r-process production could vary substantially from merger to merger.

Extreme-density stars composed of neutrons were proposed shortly after the discovery of the neutron[13], and identified with pulsars three decades later[30]. However, no spectroscopic confirmation of the composition of neutron stars has ever been made. The identification here of an element that could only have been synthesized so quickly under an extreme neutron flux provides the first direct spectroscopic evidence that neutron stars comprise neutron-rich matter.

Online content

Any methods, additional references, Nature Research reporting summaries, source data, extended data, supplementary information, acknowledgements, peer review information; details of author contributions and competing interests; and statements of data and code availability are available at https://doi.org/10.1038/s41586-019-1676-3.

1. Burbidge, E. M., Burbidge, G. R., Fowler, W. A. & Hoyle, F. Synthesis of the elements in stars. *Rev. Mod. Phys.* **29**, 547–650 (1957).
2. Siegel, D. M., Barnes, J. & Metzger, B. D. Collapsars as a major source of r-process elements. *Nature* **569**, 241–244 (2019).
3. Lattimer, J. M., Mackie, F., Ravenhall, D. G. & Schramm, D. N. The decompression of cold neutron star matter. *Astrophys. J.* **213**, 225–233 (1977).
4. Eichler, D., Livio, M., Piran, T. & Schramm, D. N. Nucleosynthesis, neutrino bursts and gamma-rays from coalescing neutron stars. *Nature* **340**, 126–128 (1989).
5. Freiburghaus, C., Rosswog, S. & Thielemann, F.-K. R-process in neutron star mergers. *Astrophys. J.* **525**, L121–L124 (1999).
6. Ji, A. P., Frebel, A., Simon, J. D. & Chiti, A. Complete element abundances of nine stars in the r-process galaxy Reticulum II. *Astrophys. J.* **830**, 93 (2016).
7. Metzger, B. D. et al. Electromagnetic counterparts of compact object mergers powered by the radioactive decay of r-process nuclei. *Mon. Not. R. Astron. Soc.* **406**, 2650–2662 (2010).
8. Barnes, J. & Kasen, D. Effect of a high opacity on the light curves of radioactively powered transients from compact object mergers. *Astrophys. J.* **775**, 18 (2013).
9. Tanvir, N. R. et al. A 'kilonova' associated with the short-duration γ-ray burst GRB 130603B. *Nature* **500**, 547–549 (2013).
10. Abbott, B. P. et al. GW170817: observation of gravitational waves from a binary neutron star inspiral. *Phys. Rev. Lett.* **119**, 161101 (2017).
11. Pian, E. et al. Spectroscopic identification of r-process nucleosynthesis in a double neutron-star merger. *Nature* **551**, 67–70 (2017).
12. Smartt, S. J. et al. A kilonova as the electromagnetic counterpart to a gravitational-wave source. *Nature* **551**, 75–79 (2017).
13. Baade, W. & Zwicky, F. Cosmic rays from supernovae. *Proc. Natl Acad. Sci. USA* **20**, 259–263 (1934).
14. Tanaka, M. & Hotokezaka, K. Radiative transfer simulations of neutron star merger ejecta. *Astrophys. J.* **775**, 113 (2013).
15. Kasen, D., Metzger, B., Barnes, J., Quataert, E. & Ramirez-Ruiz, E. Origin of the heavy elements in binary neutron-star mergers from a gravitational-wave event. *Nature* **551**, 80–84 (2017).
16. Sneden, C., Bean, J., Ivans, I., Lucatello, S. & Sobeck, J. MOOG: LTE line analysis and spectrum synthesis. *Astrophysics Source Code Library* https://www.as.utexas.edu/~chris/moog.html (2012).
17. Kerzendorf, W. E. & Sim, S. A. A spectral synthesis code for rapid modelling of supernovae. *Mon. Not. R. Astron. Soc.* **440**, 387–404 (2014).
18. Lodders, K., Palme, H. & Gail, H.-P. in *Solar System: Landolt Börnstein Group VI Astronomy and Astrophysics* Vol. 4B (ed. Trümper, J. E.) 712 (Springer, 2009).
19. Bisterzo, S., Travaglio, C., Gallino, R., Wiescher, M. & Käppeler, F. Galactic chemical evolution and solar s-process abundances: dependence on the ^{13}C-pocket structure. *Astrophys. J.* **787**, 10 (2014).
20. Honda, S., Aoki, W., Ishimaru, Y. & Wanajo, S. Neutron-capture elements in the very metal-poor star HD 88609: another star with excesses of light neutron-capture elements. *Astrophys. J.* **666**, 1189–1197 (2007).
21. Sneden, C. et al. Evidence of multiple r-process sites in the early galaxy: new observations of CS 22892–052. *Astrophys. J.* **533**, L139–L142 (2000).
22. Kasen, D., Badnell, N. R. & Barnes, J. Opacities and spectra of the r-process ejecta from neutron star mergers. *Astrophys. J.* **774**, 25 (2013).
23. Jeffery, D. J. & Branch, D. in *Supernovae, Jerusalem Winter School for Theoretical Physics* Vol. 6 (eds Wheeler, J. C., Piran, T. & Weinberg, S.) 149 (World Scientific, 1990).
24. Kurucz, R. L. Including all the lines: data releases for spectra and opacities. *Can. J. Phys.* **95**, 825–827 (2017).
25. Wanajo, S. et al. Production of all the r-process nuclides in the dynamical ejecta of neutron star mergers. *Astrophys. J.* **789**, L39 (2014).
26. Just, O., Bauswein, A., Pulpillo, R. A., Goriely, S. & Janka, H.-T. Comprehensive nucleosynthesis analysis for ejecta of compact binary mergers. *Mon. Not. R. Astron. Soc.* **448**, 541–567 (2015).
27. Drout, M. R. et al. Light curves of the neutron star merger GW170817/SSS17a: implications for r-process nucleosynthesis. *Science* **358**, 1570–1574 (2017).
28. Tanvir, N. R. et al. The emergence of a lanthanide-rich kilonova following the merger of two neutron stars. *Astrophys. J.* **848**, L27 (2017).
29. Hansen, C. J., Montes, F. & Arcones, A. How many nucleosynthesis processes exist at low metallicity? *Astrophys. J.* **797**, 123 (2014).
30. Hewish, A., Bell, S. J., Pilkington, J. D. H., Scott, P. F. & Collins, R. A. Observation of a rapidly pulsating radio source. *Nature* **217**, 709–713 (1968).
31. Sneden, C., Lawler, J. E., Cowan, J. J., Ivans, I. I. & Den Hartog, E. A. New rare earth element abundance distributions for the Sun and five r-process-rich very metal-poor stars. *Astrophys. J.* **182** (Suppl.), 80–96 (2009).
32. Sneden, C. et al. The extremely metal-poor, neutron capture-rich star CS 22892-052: a comprehensive abundance analysis. *Astrophys. J.* **591**, 936–953 (2003).

Methods

Spectral synthesis

We used different codes to compute synthetic absorption spectra, namely MOOG[16,33] v. 2014 and our own single-temperature and single-density LTE code. In addition, we verified our results using the TARDIS supernova spectral synthesis code. For the first two codes, we used line lists gathered from the literature (see Supplementary Information). For the TARDIS modelling, we used the line lists of Kurucz[24]. Our codes yield consistent results with the different line lists.

MOOG is a synthetic spectrum code normally used to generate synthetic absorption spectra of photospheres in cool stars under the assumption of local thermodynamic equilibrium. It requires a model atmosphere that dictates how temperature, gas pressure and electron density behave in different layers of the surface gas. Here we adopt Kurucz model atmospheres[34]. The second requirement is a line list that contains the rest wavelength of the absorption transition, the element or ion in which the transition takes place, the excitation potential of the lower level, and the oscillator strength. The atomic data are based on refs. [31,35–40] with updates from the National Institute of Standards and Technology (NIST). The strengths of the absorption features are calculated solving radiative transfer equations with a plane parallel treatment of the atmospheres, assuming that the velocity distribution is Maxwellian, and that excitations and ionizations are described by the Boltzmann and Saha equations, respectively. The line/wing damping follows a scaled Unsöld approximation and the source function follows a simple blackbody, while scattering (on H, He and e^-) enters mainly through opacity terms.

Our own code assumes only a gas in LTE without scattering, and that the Boltzmann and Saha equations can be used to obtain the ionization and excitation state of each element individually. We then use the line lists above and level information from NIST to determine the relative strengths of the lines. We adopt a fiducial electron density of $\log n_e = 7.8$, based on the mean density of $0.04 M_\odot$ (where $M_\odot$ is the mass of the Sun) of singly ionized material in a sphere with the area of the best-fit blackbody. The density of the atmosphere is almost certainly lower than this.

Demonstrating that the MOOG models and our LTE calculations are reasonably comparable, for the MOOG models an effective temperature (T_{eff}) at the surface of the photosphere of roughly 5,500 K and a surface gravity of log = 0 (following the temperature and density profiles in the Kurucz model atmospheres) give rise to a temperature of 3,800 K and an electron density of $n_e = 10^7$ cm^{-3} within the photosphere. Absorption lines from lanthanide ions are believed to be an important source of opacity owing to transitions with unknown oscillator strengths. For an LTE plasma, it is likely that such lines are important and create a complex continuum[15,22]. However, the lanthanide opacity is extremely high in the ultraviolet and blue regions of the spectrum. The fact that we detect blue emission in the spectrum of AT2017gfo is already a strong indication that lanthanide elements do not dominate the early-continuum spectrum, as suggested previously[41,42]. Furthermore, the infrared feature arises from levels that may be overpopulated owing to optical pumping, enhancing the strength of this feature further with respect to the line-generated continuum at these wavelengths.

Synthetic spectra are generated using both codes on the basis of line lists containing r-process elements capable of producing strong features in an LTE plasma at these temperatures. We include all elements from $_{33}$As up to $_{83}$Bi, as well as $_{90}$Th and $_{92}$U. We do not include the elements $_{35}$Se, $_{36}$Br, $_{37}$Kr, $_{53}$I and $_{54}$Xe as they produce no strong or moderate lines at these temperatures and are rarely detected in stellar spectra[43]; these elements have first excitation energies above 5.97 eV for their neutral and singly charged ions, giving a fractional population less than 10^{-8} at our fiducial temperature. Neither do we include elements with no stable isotopes ($_{43}$Tc and $_{61}$Pm), or any molecules. The absorption-line profiles are dominated by the velocity and density distribution of the expanding atmosphere.

Our line lists contain the strongest lines for LTE spectra at these temperatures. Because we are interested in finding strong, isolated lines, this procedure should effectively capture all lines that could realistically be candidates.

Could large numbers of weak lines dominate the opacity?

The opacity of the kilonova is dominated by absorption lines. The list of lines that we use for MOOG (see references above) has most of the strong lines in common with the Kurucz list[44] that we use for the TARDIS modelling. The results we retrieve from the different techniques and line lists are a useful check on the robustness of the modelling methodologies. Both methods yield consistent results, indicating that the overall result presented here is robust to the selection of the specific line list and the modelling method chosen. We note that a feature at about 810 nm is also produced in the spectral synthesis analysis of ref. [14], where lists comprising known lines are also used. This feature (M. Tanaka, private communication) is produced primarily by the same Sr II lines we identify in this work.

The major caveat in identifying line features is the possibility that missing lines could have a larger influence on the broad spectral shape than the predicted effect from known lines. Of particular concern are the large numbers of unknown lines from the lanthanide elements that are likely to dominate the line-expansion opacity[22,45]. Although we argue here that our line lists are reasonably complete in strong lines at these temperatures and densities (and given that they are used for modelling stars with similar temperatures and densities, this makes sense), it is possible that a very large number of weaker lines could contribute.

However, the line-forming region of the kilonova is likely to be physically extended, covering a substantial fraction of the kilonova radius, particularly in the near-infrared. The presence of a P Cygni profile at around 1 μm supports the idea that a substantial volume (though not mass) of the kilonova must be largely optically thin at this wavelength. The mass absorption coefficient of the Sr II lines at around 1.05 μm peaks at about 4×10^3 cm^2 g^{-1} for lines with a full width at half maximum (FWHM) of $0.01c$, a temperature of 5,000 K and a density of 10^{-13} g cm^{-3}. This is at least two orders of magnitude higher than the mean value obtained for lanthanides such as Ce and Nd in the optically thin limit using the Kurucz line lists. Given that the line lists for these elements are likely to be highly incomplete at these wavelengths, we extrapolate the value of the Ce line opacity of the Vienna Atomic Line Database (VALD) lines at 9,000 Å to be roughly 1.05 μm, which should give a similar opacity to the line lists calculated in ref. [22] with the autostructure code. When the lines are extremely optically thick, within the bulk of the kilonova in the first days, the Ce opacity is about 10 cm^2 g^{-1} (compare with ref. [22]). In the optically thin regime in the outer layers, the Ce line opacity rises by about two orders of magnitude. Using this optically thin extrapolation of the Ce lines, the Sr II opacity is still a factor of four to five times higher, not including abundance effects that are likely to make the Sr line stronger still. We show an example of this effect by calculating the expansion opacity for a low-optical-depth plasma in Extended Data Fig. 5. That calculation is purely illustrative, showing how the Sr lines can dominate the opacity when the gas has low optical depth. For a self-consistent model calculation, see the TARDIS model spectra in Extended Data Fig. 6.

Spectral modelling

In the spectra we identify what appear to be two separate emission components: first, a nearly blackbody spectrum modified by absorption features that appears to cool over time; and second, an emission component at redder wavelengths that increases in strength relative to the first component with time. These two components do not necessarily arise because of discrete ejection mechanisms, but may reflect the fact that different parts of the spectrum probe different physical depths and thus physical conditions, through the wavelength-dependent expansion opacity[8,46]. Here we focus only on the thermal component in the blue part of the spectrum and model it as a blackbody with an extended envelope. We model the second component with Gaussian emission lines in order not to bias the overall continuum fit at shorter wavelengths, but do not interpret them. However, these features clearly provide important information on the composition of the plasma and must be addressed in future studies.

The expansion velocity of the gas can be inferred from the expansion of the blackbody from the time of the explosion. Owing to the optical thickness of a blackbody, we would only be presented with the front face of the explosion. Consequently, pure absorption features in the spectrum should be blueshifted by the mean Doppler shift induced by the expansion speed of the gas. Conservatively, we allow 0.1–0.3*c* as the range of the blueshift[11,47,48], a value that depends on the details of the geometry of the system, and thus we restrict our search for lines in the first epoch to rest wavelengths of 350 nm and 810 nm multiplied by 1.1–1.3.

At the densities of the ejecta, the dominant source of opacity is expansion opacity[15,22]. This effect is able to establish an apparent thermalization through photo-equilibration of the states[49]. With wavelength-dependent opacity, the physical depth traced at each wavelength varies. Because the large majority of lines are at the blue end of the spectrum, the expansion opacity there will be higher and, conversely, the physical depth shallower. This causes the relative strength of ultraviolet/near-infrared lines to change compared with the pure LTE transmission values, with bluer absorption lines being less prominent relative to near-infrared ones. Additionally, because the population of states is photo-equilibrated, metastable states will be enhanced relative to non-metastable, as compared with LTE values[23]. It is therefore impossible, primarily because of the strongly wavelength-dependent opacity, to use a simple comparison of LTE line strengths across very different wavelengths. Instead, we use independent optical depth parameters (τ) for the two absorption feature fits here. We also use the TARDIS code (see below) to achieve a more self-consistent treatment with moving atmosphere, line-expansion opacity, which shows the simultaneous presence of the Sr II features at around 0.4 μm and 1 μm.

P Cygni modelling

The expansion velocity of the photosphere is very high (0.2–0.3*c*). At the measured temperature of the photosphere, the thermal widths of individual lines are very narrow compared with the gross velocity structure. This means that the resonance region is very small and the Sobolev approximation can be used in the Elementary Supernova model as a prescription for the absorption structure near isolated lines[23]. We use the implementation of the P Cygni profile in the Elementary Supernova from https://github.com/unoebauer/public-astro-tools, where the profile is parametrized in terms of the rest wavelength, λ_0, the optical depth of the line, τ, two scaling velocities for the radial dependence of τ, the photospheric velocity, and the maximal velocity of the ejecta. The latter two parameters specify the velocity stratification. The expansion velocity of the photosphere is simultaneously used for the relativistic Doppler correction to the blackbody temperature. In addition, because the implementation of the P Cygni profile that we are using does not include the relative population of the states in the transition, we have included a parameter for enhancement/suppression of the P Cygni emission component.

For practical reasons, we cannot fit all lines simultaneously. However, fortunately, a handful of lines provides most of the opacity. Because the relative opacity dictates the apparent strengths of the lines, we divide the spectrum into ultraviolet/blue and red/infrared regions to find the lines that will be strongest in their respective spectral region. We do this because the opacity changes so severely from the infrared to the optical (Fig. 3). We make the division at 600 nm where the opacity increases sharply; however, choosing 550 nm or 700 nm makes no difference. We then include the strongest lines in each region (all lines with a minimum strength of 20% of the strongest line). The resulting lines are the strong resonance lines from the ground state of Sr II at 407.771 nm and 421.552 nm, and the lines from the Sr II $4p^64d$ metastable states at 1,032.731 nm, 1,091.489 nm and 1,003.665 nm. These lines are all modelled using the same P Cygni profile prescription, where the relative strengths of each of the lines in the two absorption complexes are set by the LTE relations, and despite the relative simplicity of the analysis, this approach provides a surprisingly good fit to the data.

The final model that we use to fit the spectrum is a relativistically corrected blackbody photosphere absorbed by an expanding atmosphere, containing the five above-mentioned Sr II transitions, described by independent optical depths for the infrared and ultraviolet lines. The ratios of the lines internally in each set are defined by their LTE strengths. In the fitting model we also use two additional Gaussian emission lines at long wavelengths from the second emission component in order not to bias the long-wavelength continuum fit. The best-fit parameters and their associated errors are found by sampling the posterior probability distributions of the parameters, assuming flat priors on all parameters. The fitting framework used is LMFIT[50] and the sampling is done using emcee[51]. We initiate 100 samplers, each sampling for 1,000 steps. We discard the first 100 steps as a burn-in phase of the Markov chain Monte Carlo (MCMC) chains. We use the median of the marginalized posterior probability distribution as the best-fit values, and the 16th and 84th percentiles as the uncertainties. The best-fit models are shown in Fig. 4. The objective function, being highly nonlinear, causes the posterior probability distributions to be highly complex and the best-fit values difficult to optimize. However, the peaks of the distributions are well centred, meaning that the best-fit values are well constrained, regardless of the complexity of the posterior probability distribution.

Expansion velocity evolution

The fits constrain two independent parameters that can be used to infer the velocity of the ejected material: the photospheric expansion velocity, used to determine the width of the P Cygni line profile; and the blackbody radius, which scales with the square root of the observed luminosity and can be converted to an expansion velocity on the basis of the time of observation. These two parameters are uncorrelated, as supported by the MCMC posterior probability function samples, and therefore constitute two independent measurements of the same physical quantity. We show a plot of the evolution of these two parameters in Extended Data Fig. 4. The correspondence between the two estimates of the expansion velocity is striking, especially given that the ratio of the estimates is geometry dependent, and we have assumed only simple spherical symmetry here. Only the first epoch shows a somewhat discrepant value, and there we do not expect a P Cygni model to be entirely applicable. This close correspondence between the two independent measures and the reasonable values inferred further supports the validity of the line identification and the overall model.

TARDIS modelling

TARDIS[17] is a Monte Carlo radiative-transfer spectral synthesis code, in which photons are essentially propagated through an expanding atmosphere. Each photon will at any point have a probability of being absorbed by an atomic transition, this probability being based on the wavelength of the photon, the strength of the line, and the density of atomic species and electron populations. A synthetic spectrum can then be constructed by collecting the emergent photons.

To generate the synthetic spectra using TARDIS, we set up the physical models using the inferred photospheric expansion velocities at the observed epochs. For homologously expanding ejecta, the velocities of the atmosphere layers are at all times specified by the outer-edge expansion and the photospheric expansion. We use the measured photospheric expansion velocity as the inner expansion velocity and select the outer atmospheric velocity such that the bluest edge of the developed absorption profiles in the synthetic spectra match the observed ones. At present, TARDIS supports only spherically symmetric explosions, so for simplicity we adopt this geometry. The kilonova ejecta are in most cases likely to be asymmetric, owing to the preferential motion of the mass in the plane of the orbit of the two neutron stars. The neglect of deviation from spherical symmetry most likely affects the absorption profiles and the inferred mass in the atmosphere, as we could potentially only be seeing ejecta in a cone. Additionally, TARDIS assumes a single photospheric velocity across the entire wavelength range. Owing to the strong wavelength dependence of the opacity, as discussed earlier, the depth at which the photons escapes varies across the spectral coverage. Therefore, the same reservations about inferring the mass in a given shell at a given wavelength applies to the TARDIS simulations. This can be seen in effect when choosing an ejecta density that matches the absorption feature at 350 nm, because then the strength of the 810-nm absorption feature is greatly overpredicted. Conversely, selecting an ejecta density that matches the 810-nm absorption feature underpredicts the strength of the 350-nm absorption.

At each epoch, the temperature of the photosphere is chosen so that an atmosphere with no lines returns a blackbody-like spectrum that is similar to the best-fit blackbody found in simple P Cygni model fits. Both the excitation and the ionization structure of the elements in the atmosphere are set according to LTE, where we assume for simplicity a constant temperature throughout the atmosphere. This approach does not capture optical pumping of metastable states and other non-LTE effects that will change the population of the upper levels.

For the input abundances, we use the solar *r*-process abundance ratio as shown in Fig. 2, starting from $_{31}$Ga. We run the simulation in three steps, consecutively including heavier elements. For the first set of simulations, we include only the elements from $_{31}$Ga to $_{37}$Rb and, as can be seen in Fig. 2, no lines cause a substantial deviation from a pure blackbody. Next we include $_{38}$Sr, which forms the strong feature observed centred at 810 nm in the first epoch, almost exclusively owing to the three strong Sr II lines at around 1 μm. Finally we run the same simulation, including all elements from $_{31}$Ga to $_{92}$U. The feature at 810 nm is unaffected by the inclusion of the heavier elements.

For the density, we initially adopt a power-law density structure of the ejecta, parametrized in terms of velocity and epoch: $\rho(v,t) = \rho_0(t_0)^3(v/v_0)^n$. We find that the line shapes depend on the assumed slope, where for steeper slopes a larger fraction of the line absorption is closer to the line centre. We specify a density profile of $n = -3$, as in ref. [52], as this supported by the theoretical models and seems to reproduce the absorption profiles relatively well. As also investigated in ref. [15], there is some freedom in the choice of slope, as it is not well constrained from a modelling perspective and could have different values depending on the matter-ejection mechanism.

Adopting a single ρ_0 across all four epochs, with $n = -3$, does not yield synthetic spectra that match the observed spectra well around the 810-nm $_{38}$Sr absorption feature across the epochs. If ρ_0 is chosen to reproduce the strength of the $_{38}$Sr absorption feature of the first epoch, the strength of the absorption feature is greatly overpredicted in the later epochs using the same composition and assuming homology; the ejecta density has to be scaled down by a factor of five in the subsequent epochs to match the spectrum. In other words, the observed mass of Sr in the optically thin part of the spectrum inferred from the TARDIS model for the first-epoch spectrum appears to be much larger than for the later epochs. Specifically, atmosphere masses of $5 \times 10^{-5} M_\odot$, $1 \times 10^{-5} M_\odot$, $1.2 \times 10^{-5} M_\odot$ and 1.3×10^{-5} of $_{38}$Sr are required to reproduce the observed absorption feature at 810 nm for the first four epochs respectively.

These numbers should be treated with some caution as these are derived masses assuming spherical symmetry, a fixed photospheric velocity, and no correction for light travel time effects. They must be interpreted as lower limits to the total amount of material ejected, as they trace only the matter between the photospheric front and the outer atmosphere. Using the assumed solar abundances, these masses correspond to this atmosphere having approximately 1% of the total ejecta mass inferred from lightcurve modelling[15].

The TARDIS models also constrain the amount of the heavier r-process elements present in the outer, transparent layers of the ejecta. Using the solar r-process abundances with the inclusion of the heaviest elements, the TARDIS synthetic spectra exhibit almost continuous absorption up to around 6,000 Å, which is not seen in the observed spectra. This point was also touched upon earlier. The exact limit to the amount of heavy r-process material in the outer layers is difficult to infer accurately, on the basis of the simple models used, but our modelling indicates that the ratio of heavy to light element abundance in this layer is much smaller than the solar r-process ratio. This conclusion is consistent with the inference made by other authors on the basis of the early blue colour of the continuum spectrum[41,42].

The inability of a single composition and density to reproduce the spectra across the first four epochs may hint at a change in the elemental abundance ratios as the photosphere recedes further into the ejecta.

The TARDIS models demonstrate that an isolated feature observed at 810 nm can be produced by Sr and that no other known lines form this feature. Additionally, the models hint at a possible variation in the abundances as the deeper layers of the ejecta component are exposed, in line with what is suggested by some models of neutron-star mergers[53].

Exclusion of Cs I and Te I identification

The Cs I 6*s*–6*p* resonance transitions[12] would of course require Cs I to be present in the gas. But because Cs has the lowest first ionization potential of any element, the singly charged ions of other elements inevitably synthesized with Cs, such as La II, Eu II and Gd II, are millions of times more abundant than Cs I in an LTE plasma at close to the observed blackbody temperatures. This problem is even worse at temperatures that produce substantial strong lines from Te I. These other elements will cause absorption lines that are at least two orders of magnitude stronger in the same wavelength region as the proposed Cs and Te lines—for example, the 706.62 nm, 742.66 nm or 929.05 nm lines of La II, Eu II and Gd II respectively, to name one of each. The same argument holds for the excited-state transition of Te I, which has a very high excitation energy of 5.49 eV; the relative population of the Te I excited state is extremely low, less than 10^{-7}. Thus, no realistic scenario exists in which lines from either of these species can be detected without being dominated by lines from other elements that are orders of magnitude stronger.

Data availability

Work in this paper was based on observations made with European Space Observatory (ESO) telescopes at the Paranal Observatory under programmes 099.D-0382 (principal investigator E. Pian), 099.D-0622 (principal investigator P. D'Avanzo), 099.D-0376 (principal investigator S. J. Smartt) and 099.D-0191 (principal investigator A. Grado). The data are available at http://archive.eso.org.

33. MOOG spectral synthesis code. https://www.as.utexas.edu/~chris/moog.html (C. Sneden, 2017).
34. Castelli, F. & Kurucz, R. L. New grids of ATLAS9 model atmospheres. https://arxiv.org/abs/astro-ph/0405087 (2004).
35. Biémont, E. & Quinet, P. Recent advances in the study of lanthanide atoms and ions. *Physica Scripta* **T105**, 38 (2003).
36. Den Hartog, E. A., Lawler, J. E., Sneden, C. & Cowan, J. J. Improved laboratory transition probabilities for Nd II and application to the neodymium abundances of the Sun and three metal-poor stars. *Astrophys. J.* **148** (Suppl.), 543–566 (2003).
37. Lawler, J. E., Bonvallet, G. & Sneden, C. Experimental radiative lifetimes, branching fractions, and oscillator strengths for La II and a new determination of the solar lanthanum abundance. *Astrophys. J.* **556**, 452–460 (2001).
38. Lawler, J. E., Wickliffe, M. E., den Hartog, E. A. & Sneden, C. Improved laboratory transition parameters for Eu II and application to the solar europium elemental and isotopic composition. *Astrophys. J.* **563**, 1075–1088 (2001).
39. Lawler, J. E., Wickliffe, M. E., Cowley, C. R. & Sneden, C. Atomic transition probabilities in Tb II with applications to solar and stellar spectra. *Astrophys. J.* **137** (Suppl.), 341–349 (2001).
40. Lawler, J. E., Den Hartog, E. A., Sneden, C. & Cowan, J. J. Improved laboratory transition probabilities for Sm II and application to the samarium abundances of the Sun and three r-process-rich, metal-poor stars. *Astrophys. J.* **162** (Suppl.), 227–260 (2006).

41. McCully, C. et al. The rapid reddening and featureless optical spectra of the optical counterpart of GW170817, AT 2017gfo, during the first four days. *Astrophys. J.* **848**, L32 (2017).
42. Chornock, R. et al. The electromagnetic counterpart of the binary neutron star merger LIGO/Virgo GW170817. IV. Detection of near-infrared signatures of r-process nucleosynthesis with Gemini-South. *Astrophys. J.* **848**, L19 (2017).
43. Sneden, C., Cowan, J. J. & Gallino, R. in *Chemical Abundances in the Universe: Connecting First Stars to Planets* Vol. 265 (eds Cunha, K., Spite, M. & Barbuy, B.) 46–53 (IAU Symposium, 2010).
44. Kurucz line list. http://kurucz.harvard.edu/linelists/gfnew/gfall08oct17.dat.
45. Tanaka, M. et al. Properties of kilonovae from dynamical and post-merger ejecta of neutron star mergers. *Astron. Astrophys.* **852**, 109 (2018).
46. Karp, A. H., Lasher, G., Chan, K. L. & Salpeter, E. E. The opacity of expanding media—the effect of spectral lines. *Astrophys. J.* **214**, 161 (1977).
47. Shappee, B. J. et al. Early spectra of the gravitational wave source GW170817: evolution of a neutron star merger. *Science* **358**, 1574–1578 (2017).
48. Waxman, E., Ofek, E., Kushnir, D. & Gal-Yam, A. Constraints on the ejecta of the GW170817 neutron-star merger from its electromagnetic emission. *Mon. Not. R. Astron. Soc.* **481**, 3423–3441 (2018).
49. Pinto, P. A. & Eastman, R. G. The physics of type IA supernova light curves. II. Opacity and diffusion. *Astrophys. J.* **530**, 757–776 (2000).
50. Newville, M. et al. Lmfit: non-linear least-square minimization and curve-fitting for Python. *Astrophysics Source Code Library* https://zenodo.org/record/11813#.XX-EoS3MxuU (2016).
51. Foreman-Mackey, D., Hogg, D. W., Lang, D. & Goodman, J. emcee: the MCMC hammer. *Publ. Astron. Soc. Pacific* **125**, 306 (2013).
52. Tanaka, M. et al. Kilonova from post-merger ejecta as an optical and near-Infrared counterpart of GW170817. Publ. *Astron. Soc. Japan* **69**, 102 (2017).
53. Perego, A. et al. Neutrino-driven winds from neutron star merger remnants. *Mon. Not. R. Astron. Soc.* **443**, 3134–3156 (2014).

Acknowledgements We thank M. Tanaka for revisiting his previous analysis for us and for access to his spectra and line lists. We thank J. Hjorth and N. Rea for discussions. We thank the ESO Director General for allocating Director's Discretionary Time to this programme, and the ESO operation staff for support. D.W., D.B.M., and J.S. are supported in part by Independent Research Fund Denmark grant DFF-7014-00017. The Cosmic Dawn Center is funded by the Danish National Research Foundation under grant number 140. C.J.H. acknowledges support from the 'ChETEC' COST Action (CA16117), supported by COST (European Cooperation in Science and Technology). A.A. is supported by the European Research Council (ERC) through ERC Starting Grant 677912 EUROPIUM. A.A. and A.B. are supported by the Sonderforschungsbereich SFB 1245 'Nuclei: From Fundamental Interactions to Structure and Stars'. A.B. and A.K. are supported by the Sonderforschungsbereich SFB 881 'The Milky Way System' (subprojects A03, A05, A10 and A11) of the German Research Foundation (DFG). A.B. is supported by the ERC through ERC Starting Grant 759253 GreatMoves, and acknowledges support from the Klaus Tschira Foundation. S.C. acknowledges partial funding from Agenzia Spaziale Italiana-Istituto Nazionale di Astrofisica grant I/004/11/3. G.L. is supported by a research grant (19054) from Villum Fonden. K.E.H. acknowledges support by a Project Grant (162948-051) from The Icelandic Research Fund. A.J.L. acknowledges funding from the ERC under grant agreement 725246, and from the UK Science and Technologies Facilities Council (STFC) via grant ST/P000495/1. E.P. acknowledges funding from the Agenzia Spaziale Italiana (ASI) INAF grant I/088/06/0, and from the INAF project 'Gravitational Wave Astronomy with the first detections of aLIGO and aVIRGO experiments'.

Author contributions D.W., C.J.H. and J.S. were the primary drivers of the project; A.K., D.B.M., J.P.U.F. and A.C.A. were involved in discussions that developed the understanding of the physical processes. All authors contributed to discussions and to editing of the paper. D.W. did the initial blackbody with absorber fits to the first-epoch spectrum, created Figs. 1, 3 and Extended Data Fig. 3, 5, made the initial line identification, recognised the P Cygni profiles in the later epochs, wrote the LTE code, and was the primary author of the main text. C.J.H. computed the initial models and synthetic spectra with MOOG, and generated the MOOG spectra for HD 88609 and CS 22892–052. C.J.H. and A.K. produced the MOOG spectra from 3,000 Å to 20,000 Å for the kilonova template photosphere for all heavy elements. C.J.H. wrote the sections on MOOG spectrum synthesis and large parts of the text on nucleosynthesis. A.K. provided the line lists. J.S. reduced and processed all the X-shooter data, produced the P Cygni fitting codes and fit the P Cygni profiles to all epochs, as well as extending the TARDIS code to include the Kurucz line lists and implementing the TARDIS modelling. J.S. also produced Fig. 3 and Extended Data Figs. 1, 2, 6, and wrote the related Methods sections and a substantial part of the main text.

Competing interests The authors declare no competing interests.

Additional information

Supplementary information is available for this paper at https://doi.org/10.1038/s41586-019-1676-3.

Correspondence and requests for materials should be addressed to D.W.

Reprints and permissions information is available at http://www.nature.com/reprints.

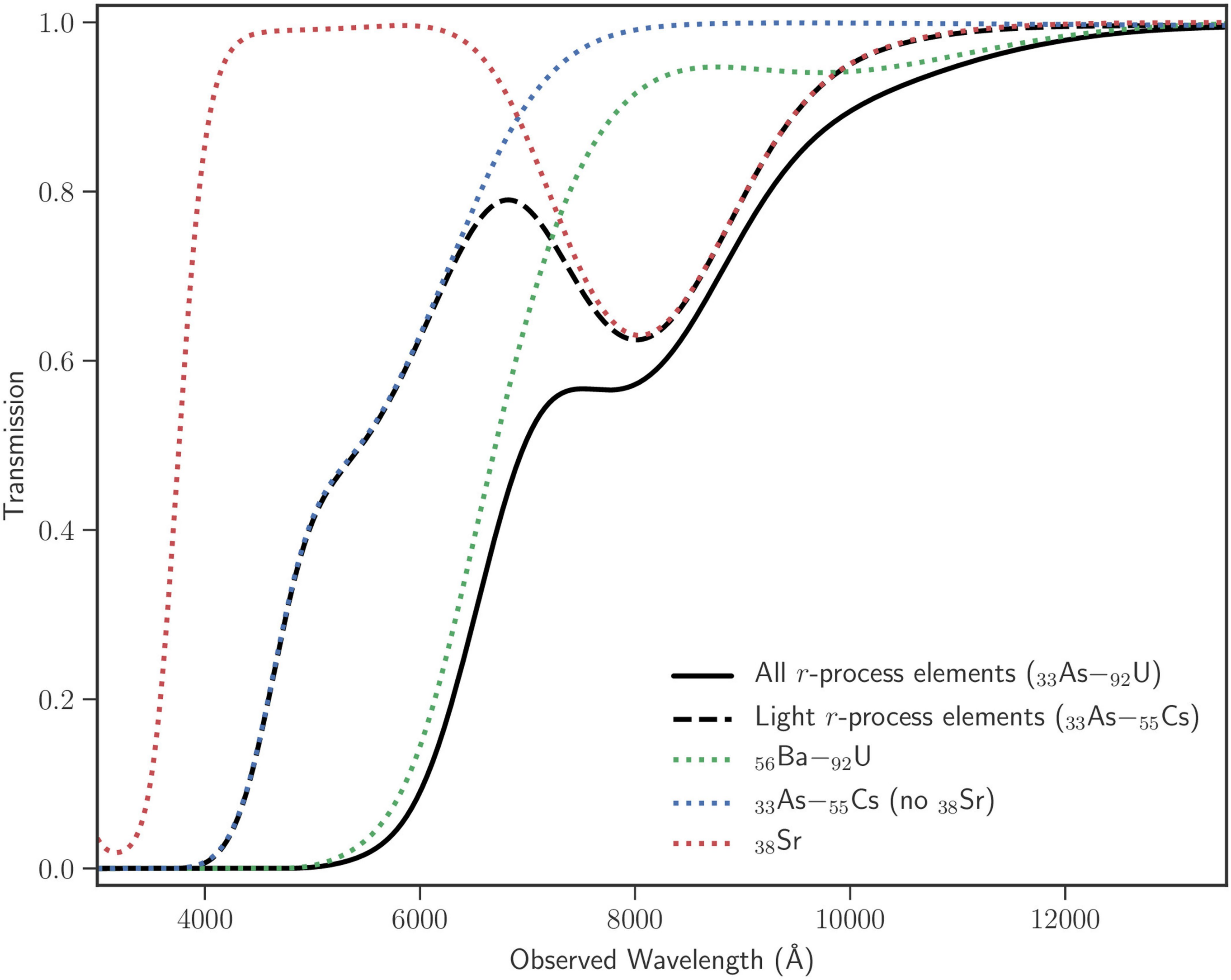

Extended Data Fig. 1 | Synthetic r-process-element transmission spectra. These spectra were generated using MOOG, in which the relative abundances are based on solar r-process abundances. The spectra were blueshifted, broadened and normalized as in Fig. 3. The solid black line is the total transmission spectrum for an atmosphere containing all the r-process elements ($_{33}$As to $_{92}$U). The dashed black line is the same spectrum, but including only the light r-process elements ($_{33}$As to $_{55}$Cs). The contributions from different subsets of species are also shown. The green dotted line shows the heavy r-process elements ($_{56}$Ba to $_{92}$U); the blue dotted line shows the light r-process elements ($_{33}$As–$_{55}$Cs) excluding Sr, which is shown as a red dotted line. This plot shows how Sr stands out in absorption, regardless of the composition of the material. The normalization is arbitrary and different to the LTE equivalent in Fig. 3 for display reasons.

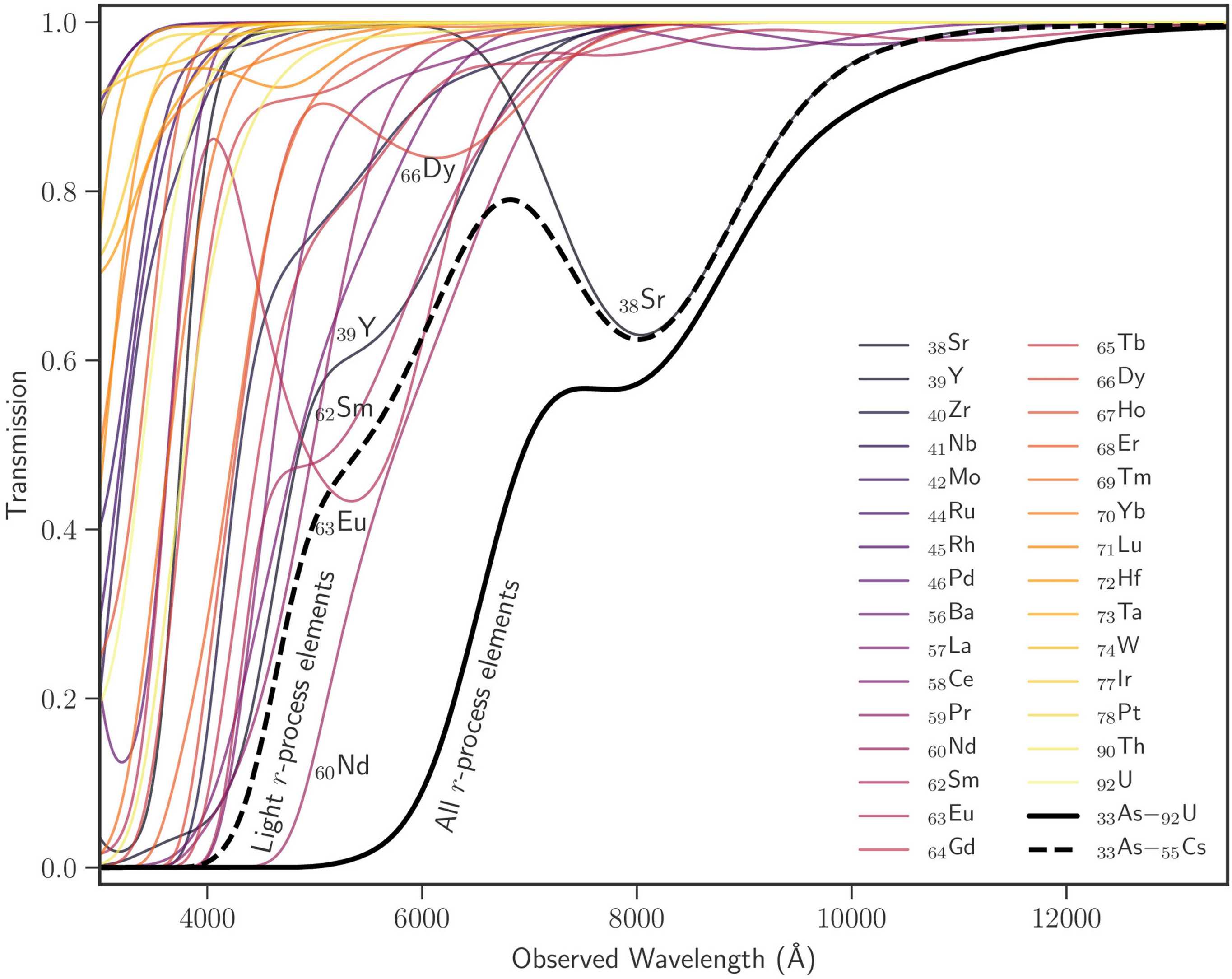

Extended Data Fig. 2 | Synthetic r-process transmission spectra. The spectra were generated with MOOG and are similar to those shown in Extended Data Fig. 1, except that all element contributions are displayed individually. The elements that contribute most at the reddest wavelengths are noted within the plotted line.

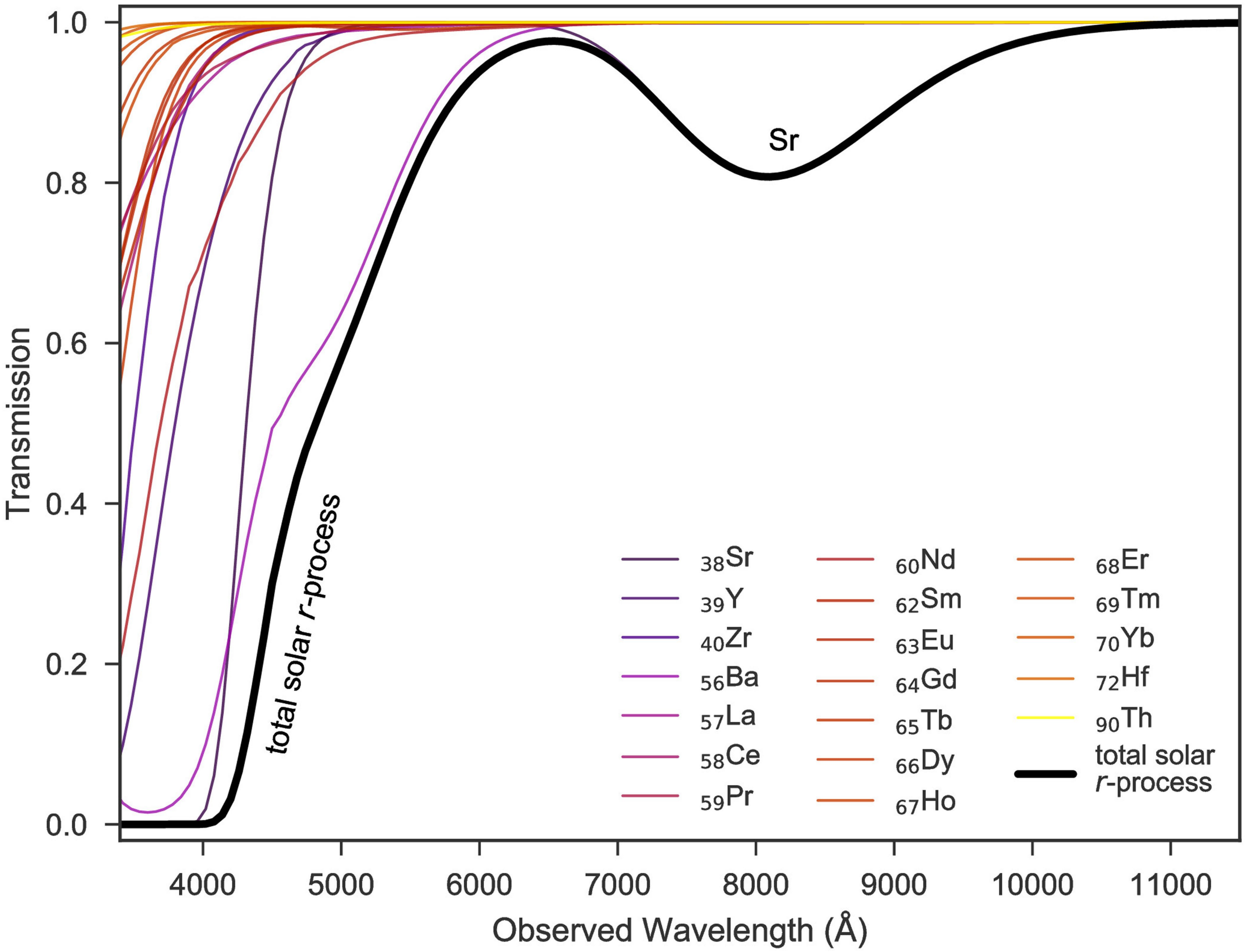

Extended Data Fig. 3 | Thermal transmission spectra for r-process elements plotted individually. The spectra are based on the lines formed in a gas in local thermal equilibrium. The abundances of elements are scaled to the solar r-process and the spectra are velocity broadened, blueshifted and normalized as in Fig. 3. The spectrum derived from the total solar r-process abundance mix is plotted as a thick black line. The contributions from Sr clearly dominate at around 8,000 Å, with no substantial contribution from any other element.

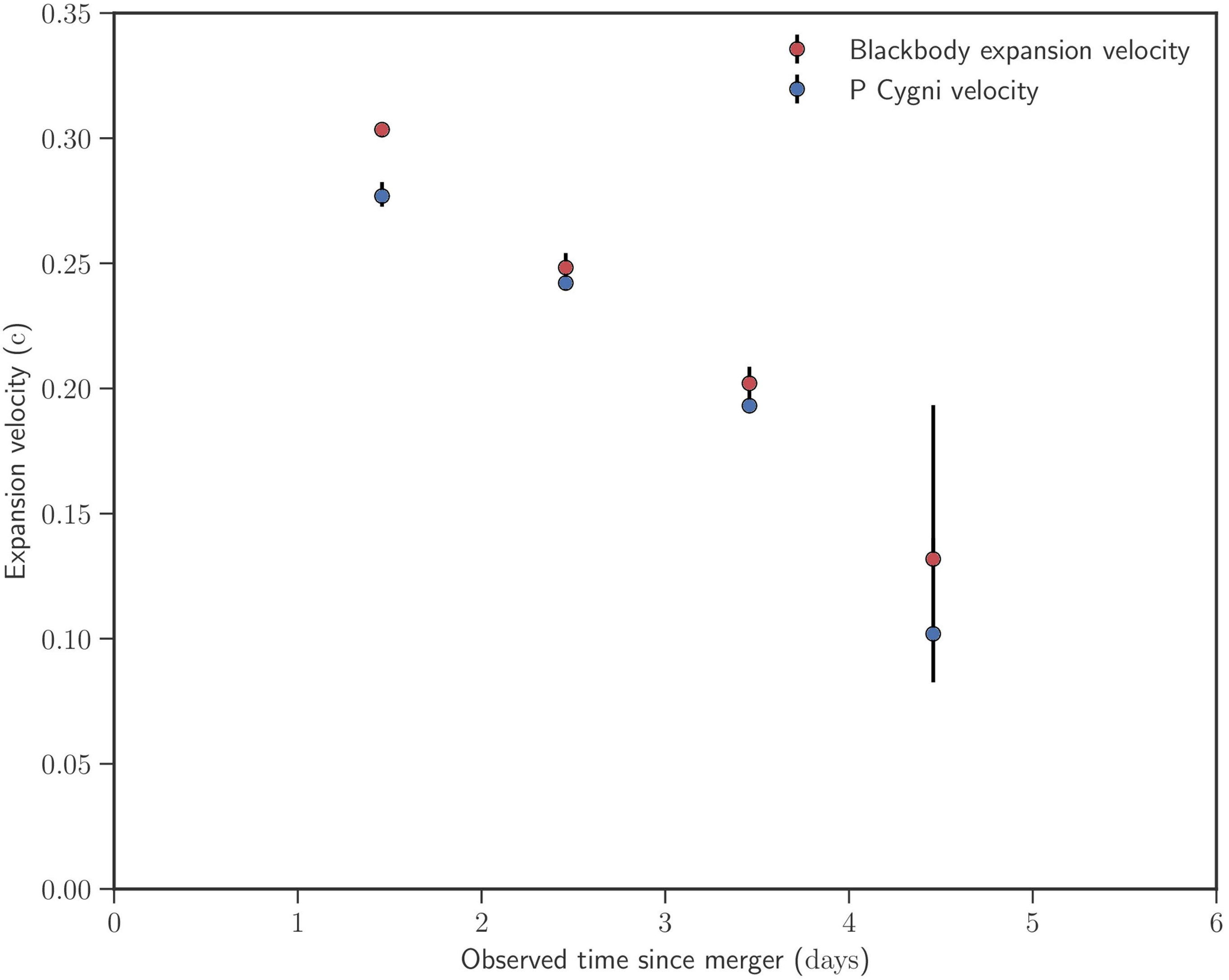

Extended Data Fig. 4 | Evolution of the ejecta expansion velocity. The velocities were determined independently from the P Cygni absorption line widths (blue points) and the blackbody radius (red points). Uncertainties shown are 1σ. The correspondence between the two independent estimates is striking.

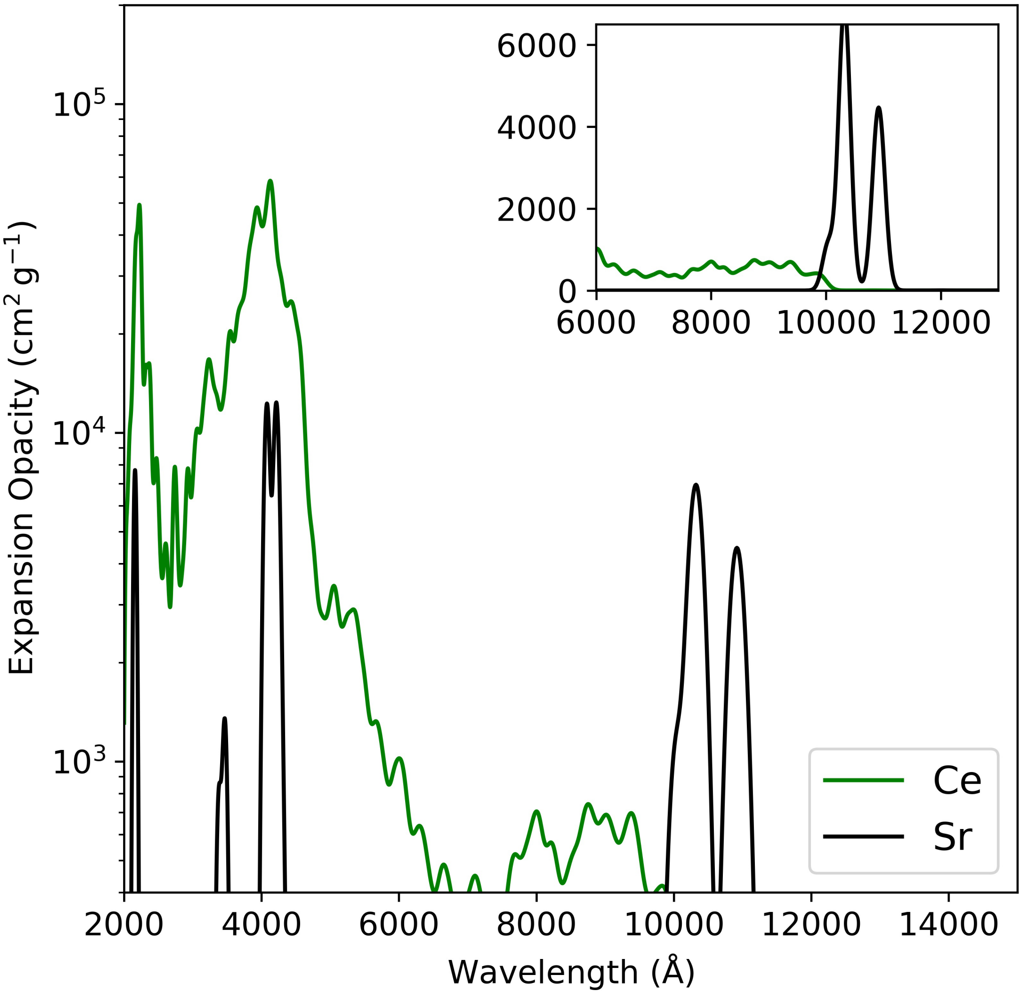

Extended Data Fig. 5 | Comparison of the expansion opacities at modest optical depths for Sr and Ce. This calculation shows the potential of Sr to dominate the opacity at around 1 µm at low optical depths. The opacities are based on LTE calculations for a gas at a temperature of 5,000 K, a mean local density of 8.4×10^{-17} g cm^{-3} for Sr or Ce, an electron density of 7.6×10^{8} cm^{-3}, and a 1% atmospheric radius at 1.5 days after the explosion. Line lists used for Sr and Ce are from the Kurucz and VALD databases respectively.

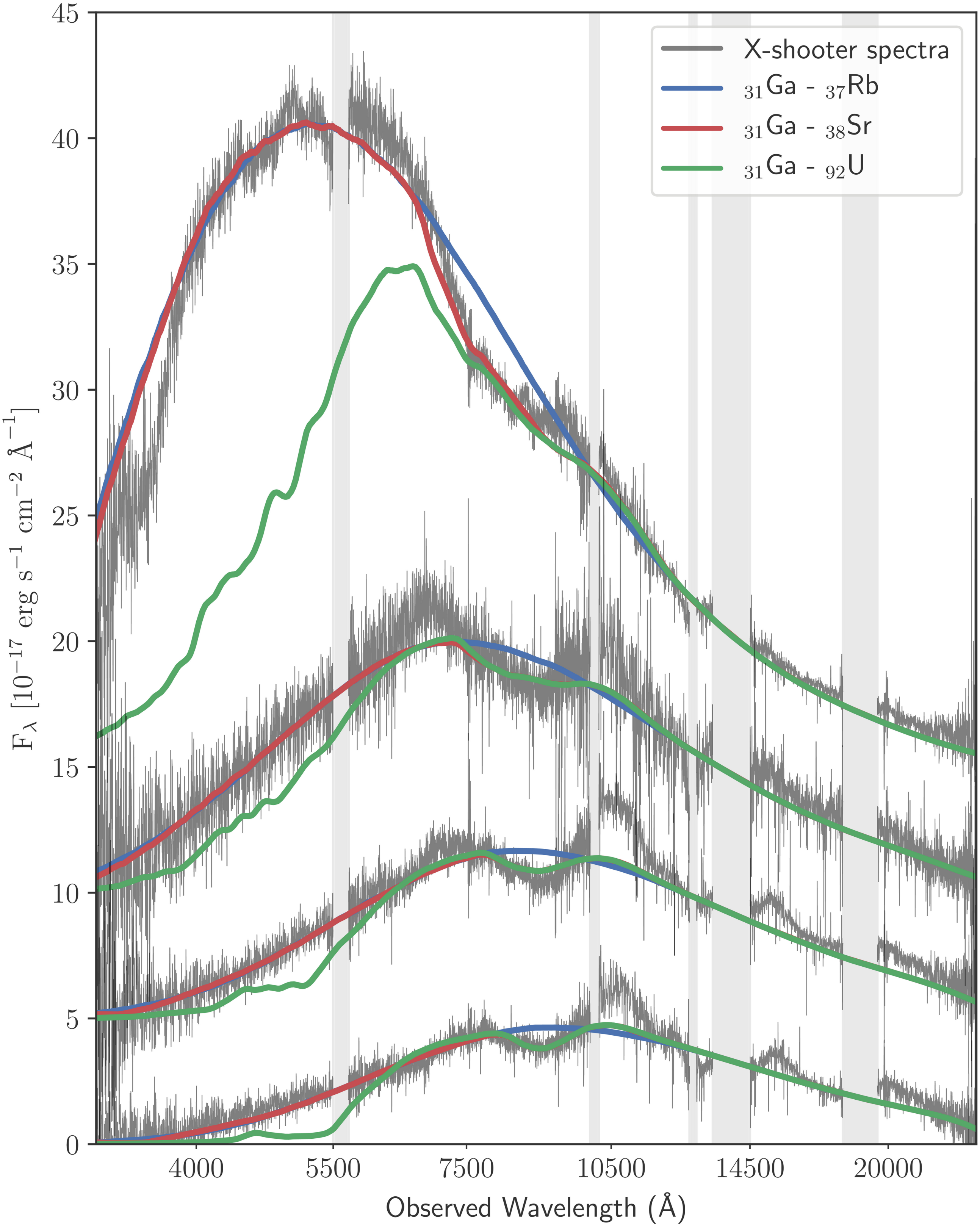

Extended Data Fig. 6 | Radiative transfer models from the first four epochs using the TARDIS code. The blue line is the synthetic TARDIS spectrum using relative solar r-process abundances and including elements from $_{31}$Ga to $_{37}$Rb—that is, without Sr. The red line also includes $_{38}$Sr. The green line is a model including all elements from $_{31}$Ga to $_{92}$U. These models show that the spectra are well reproduced with elements around the first r-process abundance peak, specifically Sr.